



OPEN

Multiphysics simulations of a cylindrical waveguide optical switch using phase change materials on silicon

Alireza Malek Mohammad¹, Mahmoud Nikoufard^{1,2}✉ & Senour Abdolghaderi²

This work presents the design and multiphysics simulation of a cylindrical waveguide-based optical switch using germanium-antimony-tellurium (GST) as an active phase change material. The innovative cylindrical architecture is theoretically analyzed and evaluated at 1550 nm wavelength for telecommunication applications. The dispersion relation is derived analytically for the first time to model the optical switch, while finite element method (FEM) and finite difference time domain (FDTD) techniques are utilized to simulate the optical modes, light propagation, and phase change dynamics. The fundamental TE_{01} and HE_{11} modes are studied in detail, enabling switching between low-loss amorphous and high-loss crystalline GST phases. Increasing the GST thickness is found to increase absorption loss in the crystalline state but also slows down phase transition kinetics, reducing switching speeds. A 10 nm GST layer results in competitive performance metrics of 0.79 dB insertion loss, 13.47 dB extinction ratio, 30 nJ average power consumption, and 3.5 Mb/s bit rate. The combined optical, thermal, and electrical simulation provides comprehensive insights towards developing integrated non-volatile photonic switches and modulators utilizing phase change materials.

Phase change materials (PCMs) based on germanium-antimony-tellurium (GST) alloys have emerged as promising candidates for photonic applications due to their unique properties. GST can reversibly and rapidly transition between amorphous and crystalline phases using electrical, optical, or thermal stimuli^{1,2}. This phase transition is non-volatile in nature. GST has three stable phases—amorphous, distorted cubic and hexagonal. The hexagonal phase exhibits higher electrical conductivity but the cubic phase has more stable optical properties, making it preferred for practical applications^{3–5}. The amorphous phase of GST has a disordered covalent bonding structure while the crystalline phase has more resonant bonding between atoms⁶. This difference in structure leads to large contrasts in optical properties like refractive index and absorption when transitioning between the phases⁷.

GST phase change materials have thus enabled several reconfigurable photonic devices including tunable color filters, absorbers, optical switches, and non-volatile photonic memories^{8–12}. Integration with metamaterials and plasmonics has allowed dynamic control over terahertz resonances and optical antennas^{6,13,14}. Harnessing the unique properties of GST and related PCMs holds great promise for integrated photonics, optical computing, and reconfigurable nanophotonics^{15–17}. However, challenges remain in improving the switching time and integrating PCMs with CMOS-compatible nanofabrication processes. Further research and innovation in materials, device design, and manufacturing is needed to fully realize the potential of these fascinating phase change materials.

Nanoscale optical switches based on phase change materials like GST have promising applications in optical neural networks and quantum information processing. For example, Rios et al.¹⁸ demonstrated a single GST device capable of storing 8 bits using near-field optical switching. Integrating GST with plasmonic nanostructures has enabled dynamic control over optical properties. Wang et al.¹⁹ showed over four times electrical modulation of reflectance at 755 nm in an electrically switchable GST antenna using a silver plasmonic strip. Ahmadvand et al.²⁰ controlled the optical response of a GST-loaded nanoparticle dimer, achieving large shifts in the resonance peak position and width. Various phase change photonic devices have been realized using GST. Wu et al.²¹ demonstrated a resonance-enhanced optical memory switch with 38 levels using sequential pulses. Wei et al.²²

¹Department of Electronics, Faculty of Electrical and Computer Engineering, University of Kashan, Kashan 8731753153, Iran. ²Nanoscience and Nanotechnology Research Center, University of Kashan, Kashan 8731753153, Iran. ✉email: mnik@kashanu.ac.ir

numerically verified a tunable GST mid-infrared absorber with 100% absorption. Wang et al.²³ and Mahmoodi et al.²⁴ simulated a low-loss, high-extinction ratio GST optical switch.

In this work, a cylindrical hybrid plasmonic optical switch using GST as the active phase change material is proposed and analyzed. The proposed structure, compatible with CMOS technology, supports the propagation of transverse electric (TE), transverse magnetic (TM), and hybrid electromagnetic modes. The field distributions of the fundamental HE_{11} and TE_{01} modes were determined by solving the Helmholtz equation, taking into account the material properties and geometrical parameters represented by the coefficients^{25–29}. Subsequently, an optimization procedure was performed to calculate the optimal thickness of each layer, maximizing the overall performance of the device. Notably, for the first time, an analytical dispersion relation for the TE_{01} mode in the proposed switch structure was derived, providing a theoretical framework for understanding the mode propagation characteristics. The validity of this analytical model was further corroborated through full-wave simulations using the finite element method (FEM), ensuring the accuracy and reliability of the theoretical predictions. Multiphysics electrical and thermal modeling of the optimized geometry identified the voltage and timing parameters needed for reversible amorphous-crystalline phase switching of the GST. Key parameters including bit rate, energy consumption, extinction ratio, and insertion loss were extracted and compared favorably to prior GST-based photonic switches. This comprehensive multiphysics analysis and optimization of a cylindrical plasmonic GST switch provides an innovative architecture and detailed understanding of the thermal, electrical, and optical characteristics essential for future integrated non-volatile nanophotonics devices and circuits.

Optical simulations

Dispersion relation of circular GST-based optical switch

Phase change materials, GST alloys, have garnered significant attention for their unique optical properties and potential applications in reconfigurable photonic devices. These chalcogenide alloys exhibit a reversible phase transformation between the amorphous and crystalline states, accompanied by a substantial change in their refractive index and optical properties. This remarkable feature forms the basis for their utilization in phase change optical switches, enabling dynamic control and modulation of light propagation. The switching mechanism involves the application of electrical pulses to induce localized heating and subsequent phase transitions in the GST material. To switch from the amorphous to the crystalline phase (SET process), a relatively high current pulse is applied, heating the GST above its crystallization temperature. This thermal annealing allows the material to crystallize, resulting in a change in its refractive index and optical properties. Conversely, to switch from the crystalline to the amorphous phase (RESET process), a shorter but higher current pulse is employed. This pulse melts the GST material, and rapid quenching causes it to solidify into an amorphous state, exhibiting a different refractive index and optical characteristics. The refractive index contrast between the amorphous and crystalline phases of GST can be leveraged to control the propagation of light within the waveguide. By strategically positioning the GST material, optical properties such as phase and intensity can be modulated, enabling dynamic reconfiguration of photonic circuits and optical signal processing functionalities.

The 2-dimensional (2D) and 3D schematic views of the proposed switch are shown in Fig. 1a,b, respectively. This cylindrical waveguide optical switch utilizes the phase change properties of GST and is designed for 1550 nm telecommunication wavelengths. As shown in Fig. 1, the switch has a cylindrical geometry with GST as the active material. When triggered, a phase transition in the GST shifts the waveguide between low loss and high loss states, thus performing optical switching. The unique cylindrical design allows for integration with fiber optics and takes advantage of the large refractive index change in GST upon switching.

The proposed optical switch consists of a cylindrical waveguide structure with four distinct layers, surrounded by SiO_2 cladding, as shown in Fig. 1. The radii of the layers are labeled *a*, *b*, *c*, and *d* respectively. Layers 1 and 3 are composed of silicon (Si) which has a refractive index $n_1 = 3.477 + i0.0002$ at the operating wavelength of 1.55 μm ^{30–34}. Layer 2 is the phase change material GST which enables switching. In its amorphous phase, GST has a

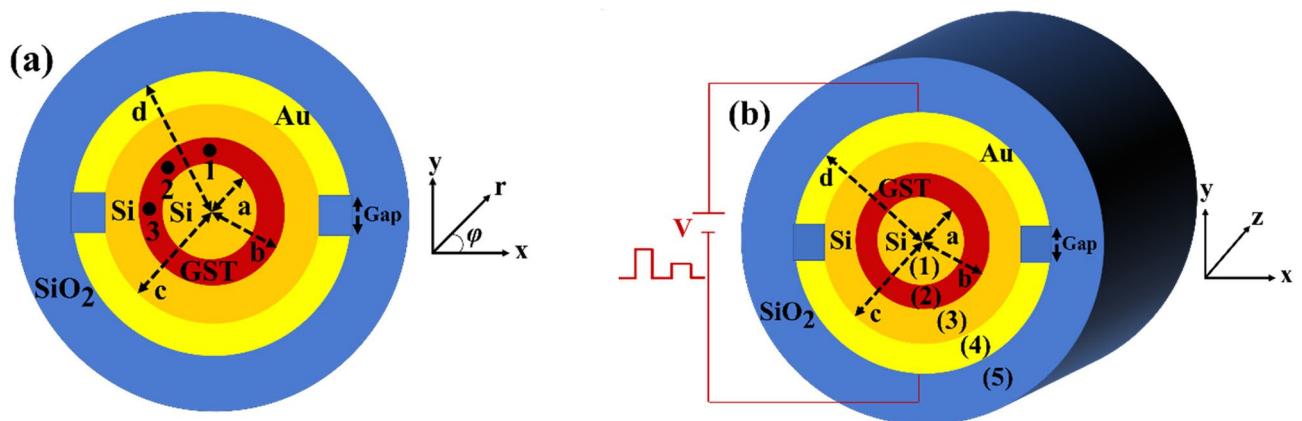


Figure 1. Cylindrical optical switch. (a) 2D cross-section of the proposed switch structure showing the GST active material surrounded by the silicon waveguide. (b) 3D view of the full optical switch device geometry.

refractive index of $n_2 = 4.6 + i0.12$, while in the crystalline phase it is $n_2 = 7.45 + i1.49^{35-37}$. The outermost layer 4 is gold (Au), patterned with two slits to form separate electrodes. Au has a refractive index of $n_4 = 0.58311 + i9.8639$ at the target wavelength³⁸⁻⁴⁰. Finally, the cladding surrounding the waveguide structure is silicon dioxide (SiO₂) which has a refractive index of $n_5 = 1.4657^{41,42}$. The refractive indices of Si, SiO₂, and both amorphous and crystalline phases of GST were accurately modeled using the well-established Sellmeier's equation, which captures the dispersion behavior of dielectric materials. For the metallic Au layer, the complex refractive index was calculated employing the Drude model, suitable for describing the optical properties of metals. In the design of GST phase change optical switches, a crucial aspect is the implementation of two distinct gaps between the electrodes. These gaps serve a critical role in electrically isolating the electrodes. Simultaneously, the gap must be sufficiently narrow to facilitate efficient and localized heating of the GST material during the switching process.

To optically analyze the proposed cylindrical switch structure, we employ a cylindrical coordinate system. The wave propagation in each layer is described by the Helmholtz equation. For simplicity in the analysis, the thin slits in the outer gold layer are neglected, as they have a negligible effect on the effective refractive index (n_{eff}) of the waveguide modes. With this approximation, the full cylindrical geometry can be analyzed using the Helmholtz equation to calculate n_{eff} and the optical properties of the propagating modes in the layered switch structure. The electric (**E**) and magnetic (**H**) fields can be determined from Helmholtz equations:

$$\begin{cases} \nabla^2 \mathbf{E} + (nk_0)^2 \mathbf{E} = \mathbf{0} \\ \nabla^2 \mathbf{H} + (nk_0)^2 \mathbf{H} = \mathbf{0} \end{cases} \quad (1)$$

where $k_0 = 2\pi/\lambda$ is the free space wave number, and λ is the free space wavelength, and n is the refractive index of each layer. In the cylindrical coordinate system, the electric (**E**) and magnetic (**H**) fields of the propagating optical waves can be expressed as:

$$\begin{cases} \mathbf{E} = E_r(r, \varphi, z)\hat{\mathbf{a}}_r + E_\varphi(r, \varphi, z)\hat{\mathbf{a}}_\varphi + E_z(r, \varphi, z)\hat{\mathbf{a}}_z \\ \mathbf{H} = H_r(r, \varphi, z)\hat{\mathbf{a}}_r + H_\varphi(r, \varphi, z)\hat{\mathbf{a}}_\varphi + H_z(r, \varphi, z)\hat{\mathbf{a}}_z \end{cases} \quad (2)$$

The electric and magnetic fields in longitudinal direction of all layers are written as follows;

$$\begin{cases} E_{zi} = E_{zi}(r, \varphi)e^{-j\gamma z} \\ H_{zi} = H_{zi}(r, \varphi)e^{-j\gamma z} \end{cases} \quad i = 1, \dots, 5 \quad (3)$$

The longitudinal field components (E_{zi} and H_{zi}) in each layer of the cylindrical waveguide structure satisfy the Helmholtz eq.:

$$\begin{cases} \nabla^2 E_{zi} + (k_i^2 - \gamma^2)E_{zi} = 0 \\ \nabla^2 H_{zi} + (k_i^2 - \gamma^2)H_{zi} = 0 \end{cases} \quad i, \dots, 5 \quad (4)$$

where $k_i = k_0 n_i$ is transverse wave number, n_i is the refractive index of each layer, and $\gamma = k_0(n_{\text{eff}} + jn_{\text{eff}})$ is the complex propagation constant. Taking advantage of the cylindrical geometry and applying the separation of variables technique, the Helmholtz Eq. (4) can be expanded as:

$$\begin{cases} \frac{d^2 E_{zi}}{dr^2} + \frac{dE_{zi}}{rdr} + \left(n_i^2 k_0^2 - \gamma^2 - \frac{m^2}{r^2}\right)E_{zi} = 0 \\ \frac{d^2 H_{zi}}{dr^2} + \frac{dH_{zi}}{rdr} + \left(n_i^2 k_0^2 - \gamma^2 - \frac{m^2}{r^2}\right)H_{zi} = 0 \end{cases} \quad i = 1, \dots, 5 \quad (5)$$

The integer m represents the azimuthal mode number and describes the φ -dependence of the fields in the cylindrical waveguide. The solutions to the Helmholtz Eq. (5) for the azimuthal field components are Bessel functions ($J(\cdot)$ and $Y(\cdot)$) in the dielectric layers (Si, and GST) and modified Bessel functions ($I(\cdot)$ and $K(\cdot)$) in the Au layer.

$$\begin{cases} E_{z1} = \left[A_{11}J_m\left(\frac{U_1}{a}r\right) + A_{12}Y_m\left(\frac{U_1}{a}r\right) \right] e^{j(-\gamma z + m\varphi)} \\ H_{z1} = \left[B_{11}J_m\left(\frac{U_1}{a}r\right) + B_{12}Y_m\left(\frac{U_1}{a}r\right) \right] e^{j(-\gamma z + m\varphi)} \\ U_1^2 = a^2(n_1 k_0^2 - \gamma^2) \geq 0 \end{cases} \quad 0 \leq r \leq a \quad (6a)$$

$$\begin{cases} E_{z2} = \left[A_{21}J_m\left(\frac{U_2}{b}r\right) + A_{22}Y_m\left(\frac{U_2}{b}r\right) \right] e^{j(-\gamma z + m\varphi)} \\ H_{z2} = \left[B_{21}J_m\left(\frac{U_2}{b}r\right) + B_{22}Y_m\left(\frac{U_2}{b}r\right) \right] e^{j(-\gamma z + m\varphi)} \\ U_2^2 = b^2(n_2 k_0^2 - \gamma^2) \geq 0 \end{cases} \quad a \leq r \leq b \quad (6b)$$

$$\begin{cases} E_{z3} = \left[A_{31}J_m\left(\frac{U_3}{c}r\right) + A_{32}Y_m\left(\frac{U_3}{c}r\right) \right] e^{j(-\gamma z + m\varphi)} \\ H_{z3} = \left[B_{31}J_m\left(\frac{U_3}{c}r\right) + B_{32}Y_m\left(\frac{U_3}{c}r\right) \right] e^{j(-\gamma z + m\varphi)} \\ U_3^2 = c^2(n_3 k_0^2 - \gamma^2) \geq 0 \end{cases} \quad b \leq r \leq c \quad (6c)$$

$$\begin{cases} E_{z4} = \left[A_{41} I_m \left(\frac{U_4}{d} r \right) + A_{42} K_m \left(\frac{U_4}{d} r \right) \right] e^{j(-\gamma z + m\varphi)} \\ H_{z4} = \left[B_{41} I_m \left(\frac{U_4}{d} r \right) + B_{42} K_m \left(\frac{U_4}{d} r \right) \right] e^{j(-\gamma z + m\varphi)} \\ U_4^2 = d^2 (n_4 k_0^2 - \gamma^2) \geq 0 \end{cases} \quad c \leq r \leq d \quad (6d)$$

$$\begin{cases} E_{z5} = \left[A_{51} I_m \left(\frac{U_5}{d} r \right) + A_{52} K_m \left(\frac{U_5}{d} r \right) \right] e^{j(-\gamma z + m\varphi)} \\ H_{z5} = \left[B_{51} I_m \left(\frac{U_5}{d} r \right) + B_{52} K_m \left(\frac{U_5}{d} r \right) \right] e^{j(-\gamma z + m\varphi)} \\ U_5^2 = d^2 (n_5 k_0^2 - \gamma^2) \geq 0 \end{cases} \quad d \leq r \quad (6e)$$

where a , b , c , and d are the radial boundaries of the cylindrical waveguide layers as labeled in Fig. 1, U_i represents the arguments of the Bessel and modified Bessel function solutions in each layer i , A and B are coefficients corresponding to the electric and magnetic field amplitudes, respectively.

The light propagation is primarily confined within layers 1–3, comprising the waveguide core regions. Consequently, Bessel functions, which are suitable for describing fields in cylindrical waveguides, are employed in Eqs. (6a–6c) to model the electric and magnetic field distributions in these layers accurately. However, in the Au and SiO₂ layers (layers 4 and 5, respectively), the optical fields decay exponentially due to the metallic and dielectric nature of these materials. To account for this evanescent behavior, modified Bessel functions, which capture the exponential decay, are utilized in Eqs. (6d) and (6e) to describe the field distributions within these layers accurately. The optical field solutions can be simplified using the following boundary conditions: at $r=0$, the fields must be finite, requiring $A_{12}=B_{12}=0$, and as $r \rightarrow \infty$, the fields decay to zero, requiring $A_{51}=B_{51}=0$. To simplify the dispersion relation calculation, we set $m=0$ and consider the TE_{0*u*} mode. This azimuthally symmetric mode has no angular field dependence, providing physical insight while enabling straightforward analysis. Applying Maxwell's equations, the transverse electric and magnetic field components (E_{ri} , $H_{\phi i}$) in each layer can be determined from the corresponding longitudinal components (E_{zi} , H_{zi}) as:

$$\begin{cases} E_{\phi 1} = \frac{j}{(U_1/a)} \mu_0 \omega \left[B_{11} J_1 \left(\frac{U_1}{a} r \right) \right] e^{-j\gamma z} \\ H_{r1} = \frac{j}{(U_1/a)} \gamma \left[B_{11} J_1 \left(\frac{U_1}{a} r \right) \right] e^{-j\gamma z} \end{cases} \quad 0 \leq r \leq a \quad (7a)$$

$$\begin{cases} E_{\phi 2} = \frac{j}{(U_2/b)} \mu_0 \omega \left[B_{21} J_1 \left(\frac{U_2}{b} r \right) + B_{22} Y_1 \left(\frac{U_2}{b} r \right) \right] e^{-j\gamma z} \\ H_{r2} = \frac{j}{(U_2/b)} \gamma \left[B_{21} J_1 \left(\frac{U_2}{b} r \right) + B_{22} Y_1 \left(\frac{U_2}{b} r \right) \right] e^{-j\gamma z} \end{cases} \quad a \leq r \leq b \quad (7b)$$

$$\begin{cases} E_{\phi 3} = \frac{j}{(U_3/c)} \mu_0 \omega \left[B_{31} J_1 \left(\frac{U_3}{c} r \right) + B_{32} Y_1 \left(\frac{U_3}{c} r \right) \right] e^{-j\gamma z} \\ H_{r3} = \frac{j}{(U_3/c)} \gamma \left[B_{31} J_1 \left(\frac{U_3}{c} r \right) + B_{32} Y_1 \left(\frac{U_3}{c} r \right) \right] e^{-j\gamma z} \end{cases} \quad b \leq r \leq c \quad (7c)$$

$$\begin{cases} E_{\phi 4} = \frac{j}{(U_4/d)} \mu_0 \omega \left[B_{41} I_1 \left(\frac{U_4}{d} r \right) + B_{42} K_1 \left(\frac{U_4}{d} r \right) \right] e^{-j\gamma z} \\ H_{r4} = \frac{j}{(U_4/d)} \gamma \left[B_{41} I_1 \left(\frac{U_4}{d} r \right) + B_{42} K_1 \left(\frac{U_4}{d} r \right) \right] e^{-j\gamma z} \end{cases} \quad c \leq r \leq d \quad (7d)$$

$$\begin{cases} E_{\phi 5} = \frac{j}{(U_5/d)} \mu_0 \omega \left[B_{51} K_1 \left(\frac{U_5}{d} r \right) \right] e^{-j\gamma z} \\ H_{r5} = \frac{j}{(U_5/d)} \gamma \left[B_{51} K_1 \left(\frac{U_5}{d} r \right) \right] e^{-j\gamma z} \end{cases} \quad d \leq r \quad (7e)$$

To satisfy the boundary conditions at each interface ($r=a$, $r=b$, $r=c$, and $r=d$), the longitudinal magnetic field H_z must be continuous across the layer boundaries. By matching H_z at these interfaces, the number of unknown field coefficients can be reduced by half.

$$\text{If } r = a, H_{z1} = H_{z2} \quad \text{then} \quad B_{11} = \frac{B_{21} J_0 \left(\frac{U_2}{b} a \right) + B_{22} Y_0 \left(\frac{U_2}{b} a \right)}{J_0(U_1)} \quad (8a)$$

$$\text{If : } r = b, H_{Z2} = H_{Z3} \text{ then } B_{31} = \frac{B_{21}J_0(U_2) - B_{32}K_0\left(\frac{U_3}{c}b\right) + B_{22}Y_0(U_2)}{I_0\left(\frac{U_3}{c}b\right)} \quad (8b)$$

If : $r = c, H_{z3} = H_{z4}$ then

$$B_{41} = \frac{B_{21}F_{11} + B_{22}F_{21} + B_{32}F_{31} + B_{42}F_{41}}{J_0\left(\frac{U_3}{c}b\right)I_0\left(\frac{U_4}{d}c\right)} \quad (8c)$$

$$F_{11} = J_0(U_2)J_0(U_3), F_{21} = Y_0(U_2)J_0(U_3) \quad (8d)$$

$$F_{31} = J_0\left(\frac{U_3}{c}b\right)Y_0(U_3) - J_0(U_3)Y_0\left(\frac{U_3}{c}b\right) \quad (8e)$$

$$F_{41} = -J_0\left(\frac{U_3}{c}b\right)K_0\left(\frac{U_4}{d}c\right) \quad (8f)$$

If : $r = d, H_{z4} = H_{z5}$ then

$$B_{51} = \frac{B_{21}F_{12} + B_{22}F_{22} + B_{32}F_{32} + B_{42}F_{42}}{J_0\left(\frac{U_3}{c}b\right)I_0\left(\frac{U_4}{d}c\right)K_0\left(\frac{U_5}{d}c\right)} \quad (8g)$$

$$F_{12} = J_0(U_2)J_0(U_3)I_0(U_4), F_{22} = Y_0(U_2)J_0(U_3)I_0(U_4) \quad (8h)$$

$$F_{32} = J_0\left(\frac{U_3}{c}b\right)Y_0(U_3)I_0(U_4) - Y_0\left(\frac{U_3}{c}b\right)J_0(U_3)I_0(U_4) \quad (8i)$$

$$F_{42} = J_0\left(\frac{U_3}{c}b\right)I_0\left(\frac{U_4}{d}c\right)K_0(U_4) - J_0\left(\frac{U_3}{c}b\right)I_0(U_4)K_0\left(\frac{U_4}{d}c\right) \quad (8j)$$

Similarly, applying boundary conditions requiring continuity of the transverse electric field E_ϕ across each interface allows determining the remaining unknown field coefficients. This can be achieved by solving the matrix equation:

$$[M][C] = [0] \rightarrow \begin{bmatrix} a_{11} & a_{12} & 0 & 0 \\ a_{21} & a_{22} & a_{23} & 0 \\ a_{31} & a_{32} & a_{33} & a_{34} \\ a_{41} & a_{42} & a_{43} & a_{44} \end{bmatrix} \begin{bmatrix} B_{21} \\ B_{22} \\ B_{32} \\ B_{42} \end{bmatrix} = [0] \quad (9)$$

Applying the boundary conditions and solving for the field coefficients, the dispersion relation for the cylindrical waveguide optical switch can finally be derived as:

$$\det(M) = a_{11}a_{22}a_{33}a_{44} - a_{11}a_{22}a_{34}a_{43} - a_{11}a_{23}a_{32}a_{44} + a_{12}a_{21}a_{33}a_{44} + a_{12}a_{21}a_{34}a_{43} - a_{12}a_{23}a_{34}a_{41} + a_{11}a_{23}a_{34}a_{42} = 0 \quad (10)$$

The dispersion relation Eq. (10) was numerically solved to obtain the complex propagation constant γ for the supported modes. The first non-trivial solution corresponds to the fundamental HE_{11} mode. With γ determined, all the field coefficients can be calculated in terms of a single reference coefficient using Eqs. 8,9. The full 2D field profiles of H_z , E_r , and E_ϕ can then be evaluated across the cylindrical waveguide cross-section.

The optimal thickness of the different layers

To optimize the inner Si layer thickness (layer 1), simulations were performed by sweeping this parameter from 100 to 1000 nm. The GST (layer 2), outer Si (layer 3), Au (layer 4) layers and gap thickness were fixed at 10 nm, 500 nm, 100 nm, and 1200 nm, respectively. The effective refractive index (n_{eff}) was calculated for the HE_{11} and TE_{01} modes, which have the lowest cutoff frequencies. A minimum Au thickness of 20 nm is required considering the electromagnetic field penetration depth, while a thickness of 100 nm is chosen to facilitate efficient heat transfer during the switching process involving the phase transition of the GST layer^{43,44}. The 1200 nm gap thickness has a negligible effect on n_{eff} but enables heat confinement for phase change⁴³.

Figure 2a,b shows the simulated $\text{Re}(n_{\text{eff}})$ and $\text{Im}(n_{\text{eff}})$ parts of the effective refractive index and confinement factor (Γ) as a function of the inner Si layer thickness ($0 \leq r \leq a$) for both amorphous and crystalline phases of the GST material. As shown in Fig. 2a, $\text{Re}(n_{\text{eff}})$ increases for both HE_{11} and TE_{01} modes as the inner Si layer (layer 1) thickness grows from 100–500 nm for both amorphous and crystalline GST phases. In this thickness

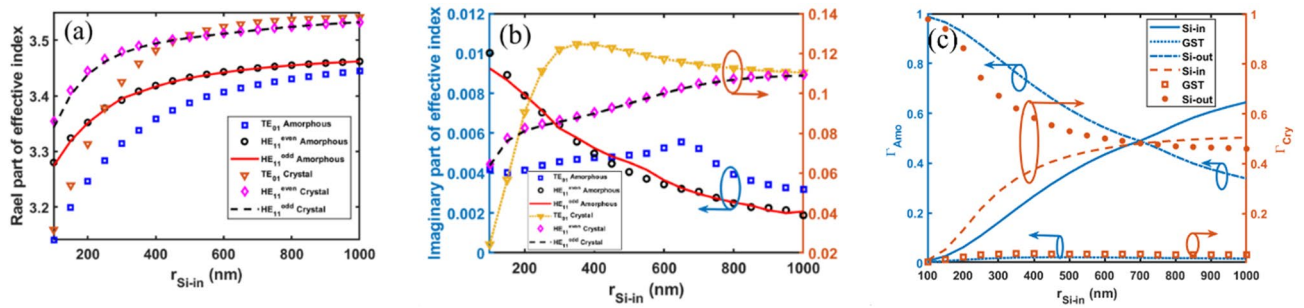


Figure 2. Effective refractive index of the proposed optical switch. (a) Real and (b) imaginary parts are shown for the fundamental HE₁₁ and TE₀₁ modes in both amorphous and crystalline phases of the GST material (c) confinement factor (Γ) of different layers for both amorphous and crystalline phases of the GST material of TE₀₁ mode.

range, optical power transfers to the inner Si layer, which can be confirmed by Fig. 2c. Above 500 nm, $\text{Re}(n_{\text{eff}})$ saturates as the optical power becomes confined in the inner Si. The refractive index of crystalline GST is higher than amorphous GST, so $\text{Re}(n_{\text{eff}})$ is greater in the crystalline phase. As the inner Si layer gets thicker, $\text{Re}(n_{\text{eff}})$ approaches the Si index since more electromagnetic fields become concentrated in layer 1. Figure 2b shows $\text{Im}(n_{\text{eff}})$ for the TE₀₁ and HE₁₁ modes. The trends depend on how the optical power becomes distributed between the GST and inner Si layers. For the HE₁₁ mode, $\text{Im}(n_{\text{eff}})$ decreases with increasing inner Si thickness in the amorphous GST phase, while it increases for crystalline GST. However, $\text{Im}(n_{\text{eff}})$ behaves differently for the TE₀₁ mode—it initially increases then decreases with increasing inner Si thickness for both GST phases. This distinct behavior arises from differences in how the optical field becomes concentrated within the GST layer for each mode. Figure 2c depicts the confinement factors of different layers as a function of the inner Si layer thickness for both amorphous and crystalline phases of the GST material, considering the TE₀₁ mode. As the inner Si layer thickness increases, a larger fraction of the optical power is confined within this layer, while the confinement factor in the GST layer remains relatively constant. Consequently, the optical power confinement in the outer Si layer decreases, correspondingly.

To optimize the outer Si layer thickness ($b < r < c$), simulations were performed sweeping this parameter from 250 to 1000 nm. The other layers were fixed with the following thicknesses: GST at 10 nm (layer 2), inner Si (layer 1) at 500 nm, Au (layer 4) at 100 nm, and gap at 1200 nm. Figure 3a,b shows the simulated $\text{Re}(n_{\text{eff}})$ and $\text{Im}(n_{\text{eff}})$ as a function of outer Si thickness for the TE₀₁ and HE₁₁ modes. In the amorphous GST phase, $\text{Re}(n_{\text{eff}})$ increases smoothly with outer Si (layer 3) thickness for both modes. For crystalline GST, $\text{Re}(n_{\text{eff}})$ rises until 500 nm thickness of outer Si, then saturates. Because the optical power concentrates in the outer Si layer for both phases, as shown in Fig. 3c. Guided modes only exist above 250 nm outer Si thickness and below this value, the TE₀₁ and HE₁₁ modes cannot be supported. The imaginary part of the effective refractive index ($\text{Im}(n_{\text{eff}})$) decreases as the outer Si thickness increases and then saturates for both phases of GST and for both TE₀₁ and HE₁₁ modes. This saturation behavior suggests that beyond a certain thickness, increasing the outer Si layer does not significantly alter the optical field distribution within the waveguide structure. Figure 3c illustrates the confinement factors of different layers as a function of the outer Si layer thickness for both amorphous and crystalline phases of the GST material, considering the TE₀₁ mode. As the outer Si thickness increases, the optical power confinement in the outer Si layer increases, while the confinement factors in the GST and inner Si layers decrease, correspondingly.

Based on the trends in Fig. 2,3, the inner and outer Si layer thicknesses are set at 500 nm and 1000 nm, respectively, where the $\text{Re}(n_{\text{eff}})$ is saturated. This provides optimal performance for amorphous and crystalline GST phases.

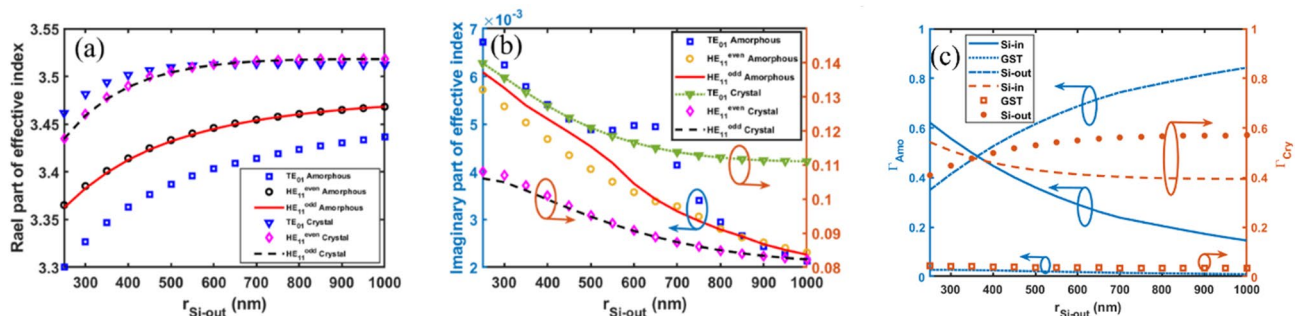


Figure 3. Effective refractive index of the proposed optical switch as a function of outer Si layer thickness. (a) Real and (b) imaginary parts are shown for the HE₁₁ and TE₀₁ modes in both amorphous and crystalline phases of the GST (c) confinement factor (Γ) of different layers for both amorphous and crystalline phases of the GST material of TE₀₁ mode.

To determine the optimal GST layer thickness, simulations were performed sweeping this parameter from 10 to 100 nm. The Au metal layer and gap dimensions were fixed at 100 nm, and 1200 nm, respectively. Figure 4 shows $\text{Re}(n_{\text{eff}})$ and $\text{Im}(n_{\text{eff}})$ as a function of the GST layer thickness. As depicted in Fig. 4a, for the crystalline phase of GST, $\text{Re}(n_{\text{eff}})$ increases toward the refractive index of the GST layer with increasing GST thickness for both HE_{11} and TE_{01} modes. This behavior is attributed to enhanced optical confinement within the GST layer. Conversely, in the amorphous phase, $\text{Re}(n_{\text{eff}})$ exhibits minimal dependence on GST thickness due to the relatively small increase in optical power confinement within the GST layer. Figure 4b shows $\text{Im}(n_{\text{eff}})$ rises with increasing GST thickness for both phases and modes, indicating higher optical loss. The loss is much greater in crystalline versus amorphous GST for example about 46 times higher at 50 nm GST thickness. This enables switching between crystalline and amorphous phases. Figure 4c depicts the confinement factor of different layers as a function of the GST layer thickness. As the GST layer thickness increases, the confinement factor within the GST layer rises, while the optical power confinement in the outer Si layer decreases. Maximal power confinement in the inner Si layer occurs at GST thicknesses of 20 nm and 60 nm for the crystalline and amorphous phases, respectively. However, a trade-off between switching speed and GST layer thickness led to the selection of a 10 nm thickness for the GST layer.

To determine the optimal Au layer thickness ($c < r < d$), simulations were performed sweeping this parameter from 10 to 100 nm. The gap distance was fixed at 1200 nm. The simulation results varying the Au layer thickness has minimal effect on $\text{Re}(n_{\text{eff}})$ and $\text{Im}(n_{\text{eff}})$ for both GST phases and modes, as shown in supplementary. This indicates negligible optical power propagates in the Au layer, which is due to the optimization of the inner and outer Si layer thicknesses. Based on these results and thermal simulations in the next section, the Au thickness is set to 100 nm. This enables voltage application without melting the electrodes^{45,46}.

To determine the optimal gap thickness, simulations were performed sweeping this dimension from 100 to 1000 nm. The results, as shown in the supplementary Fig. s2, indicate that increasing the gap thickness has a negligible effect on the $\text{Re}(n_{\text{eff}})$ and $\text{Im}(n_{\text{eff}})$ for both amorphous and crystalline phases of the GST material. This suggests that the gap does not substantially alter the optical modes within the simulated range. However, the main role of the gap is to divide the Au layer, enabling the formation of electrodes for applying the voltage required for electrical switching. Since both Au and crystalline GST absorb optical power, the gap thickness is selected as 1200 nm. This value minimizes absorption losses while providing sufficient space for the electrode integration. The chosen gap dimension of 1200 nm facilitates efficient electrical switching by allowing localized heat generation within the GST layer, without perturbing the optical properties of the waveguide modes. This optimal design ensures reliable phase transition and switching capabilities while maintaining the desired optical performance.

Longitudinal and lateral optical simulations of the cylindrical switch

To examine the optical power distribution of the TE_{01} (even and odd) and HE_{11} modes in both amorphous and crystalline GST phases, simulations were performed as shown in Fig. 5. The previously optimized layer thicknesses were used to calculate the field patterns for each mode. Comparing the amorphous and crystalline results provides insight into how the phase change affects modal confinement. Figure 5 shows the simulated optical power distribution and electric field directions across the 2D switch structure. Figure 5a,b show the TE_{01} mode in amorphous and crystalline GST, respectively. In the crystalline phase, optical power is strongly confined in the GST layer, while in the amorphous phase it is distributed across both the GST and outer Si (layer 3). The imaginary part of the effective index is 46 times higher in crystalline versus amorphous GST. For the even and odd HE_{11} modes, optical power is uniformly distributed between the inner Si (layer 1) and GST layers for amorphous GST (Fig. 5c,e), while it localizes in the GST for crystalline (Fig. 5d,f). The effective indices for all modes and phases are listed in Table 1. The localization of optical power within the GST and/or Si layers is discussed in the previous subsection, where the layer thicknesses were varied and their impact on the effective refractive index was analyzed.

Figure 6 shows the magnetic field profile along the radial direction for the TE_{01} mode, calculated both numerically using FEM and analytically using Eqs. (1–10). For the analytical approach, the propagation constant γ was derived by solving the equations. This γ was substituted back into the field expressions and plotted in MATLAB software. Comparing the two methods, helps verify the accuracy of the proposed switch model and

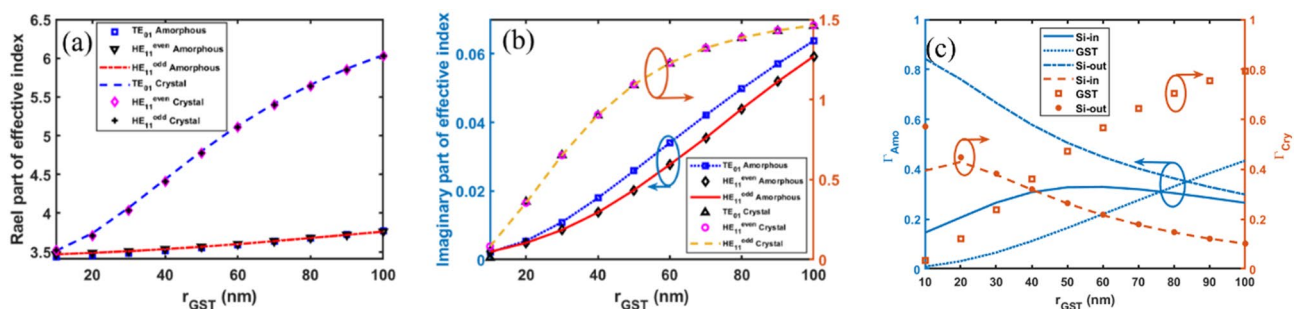


Figure 4. Effective refractive index of the proposed optical switch as a function of GST layer thickness. (a) Real and (b) imaginary parts are shown for the HE_{11} and TE_{01} modes in both amorphous and crystalline GST phases (c) confinement factor (Γ) of different layers for both amorphous and crystalline phases of the GST material of TE_{01} mode.

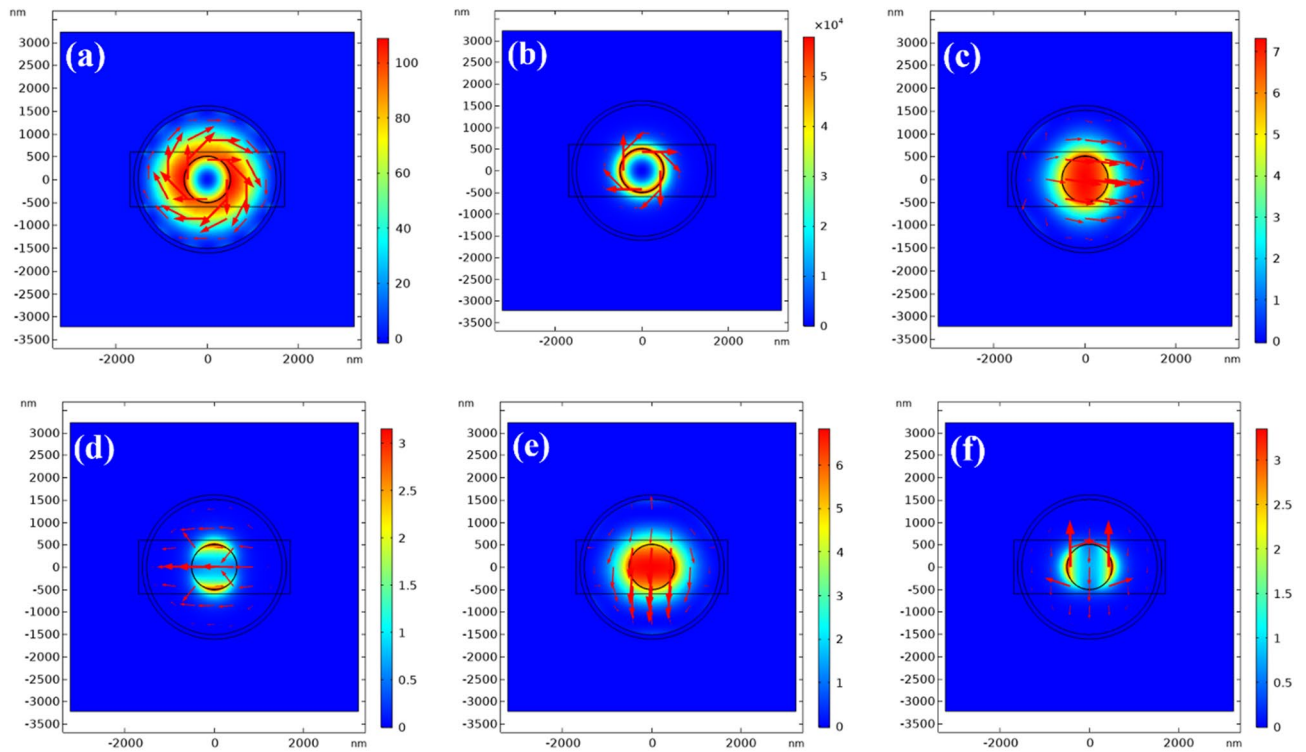


Figure 5. Optical power distribution for the TE_{01} and HE_{11} modes. TE_{01} mode in the (a) amorphous and (b) crystalline GST phases. Even HE_{11} mode pattern in the (c) amorphous and (d) crystalline phases. Odd HE_{11} mode pattern in the (e) amorphous and (f) crystalline phases. Peaks of optical power in x - or y -direction define the even and odd pattern. Arrows show the electrical field directions.

N_{eff}	Amorphous	Crystalline
TE_{01}	3.4369 + i0.0024126	3.5121 + i0.11104
HE_{11} (even)	3.4683 + i0.0022628	3.5181 + i0.082271
HE_{11} (odd)	3.4682 + i0.0023114	3.5181 + i0.082307

Table 1. Effective refractive index at 1.55 μm wavelength for the TE_{01} , even HE_{11} , and odd HE_{11} modes in the optimized cylindrical waveguide switch design. Results are shown for both amorphous and crystalline phases of the GST layer.

optimized design parameters. In the amorphous GST phase, the radial magnetic field (H_r) continuously increases from $r=0$ to 510 nm, corresponding to the inner Si layer (layer 1). It then decreases in the GST layer (layer 2), reaching zero in the Au metal region (layer 4) between 1500–1600 nm. The crystalline GST phase follows a similar trend, with the key difference that the field steeply drops to zero within the GST layer itself. The numerically simulated H_r reaches zero at 1467 nm radius, while the analytically derived field extends slightly further to 1550 nm radius before becoming zero. As shown in Table 2, the average difference between the theoretical and numerically simulated results is about 0.04% for the $\text{Re}(n_{eff})$ and 0.3% for the $\text{Im}(n_{eff})$. Based on Table 2 and Fig. 6, the analytical model shows close agreement with the finite element method (FEM) simulations, with only a small difference between the two approaches.

To determine the appropriate optical switch length, light propagation simulations were performed using the finite-difference time-domain (FDTD) method. Figure 7 shows the simulated optical power along the xz -plane for the even HE_{11} and TE_{01} modes in both amorphous and crystalline GST phases. Analyzing the power distribution along the length helps identify the minimum length needed for efficient optical switching. The comparison between amorphous and crystalline phases also reveals differences in optical confinement that impact device length. In the amorphous GST phase, Fig. 7a,c show light propagates through the switch with minimal loss. However, in the crystalline phase (Fig. 7b,d), significant loss occurs, with the power fully decayed after a few micrometer. Figure 7a indicates the HE_{11} mode power is primarily confined in the inner Si layer (layer 1). In contrast, Fig. 7c shows the TE_{01} mode propagates around the GST layer (layer 2). Figure 8 shows the simulated optical power propagation along the switch length for the HE_{11} and TE_{01} modes in the GST crystalline and amorphous phases at the midpoint of the inner Si and outer Si layers, respectively. In the amorphous phase, the optical power drops about 30% for both modes within a 20 μm length. However, in the crystalline phase

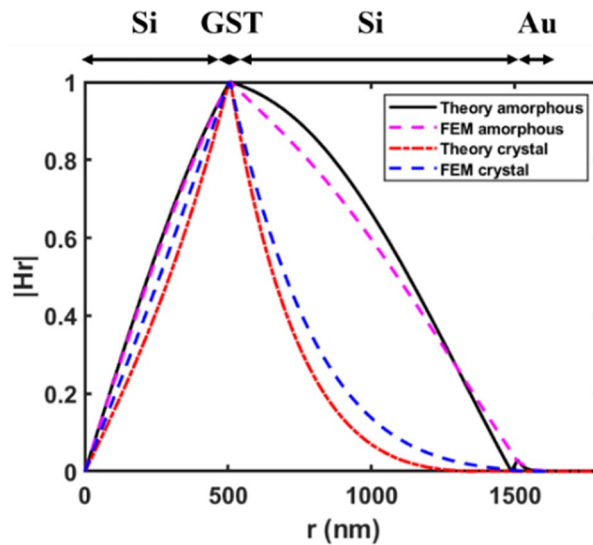


Figure 6. Radial magnetic field profile H_r for the TE_{01} mode in amorphous and crystalline GST phases. The profiles are determined analytically using Eqs. (1–10) and numerically using FEM.

	Amorphous	Crystalline
N_{eff} (Theory)	3.43392 + i0.00199	3.51236 + i0.11116
N_{eff} (FEM)	3.43630 + i0.00198	3.51220 + i0.11105
γ (Theory)	13.91997e + 3 + i8.06680e + 3	14.23794e + 6 + i450.60573e + 3
γ (FEM)	13.92962e + 3 + i8.02626e + 3	14.23729e + 6 + i450.15982e + 3

Table 2. Comparison of N_{eff} and γ for the TE_{01} mode in the optimized optical switch design. Results are shown at 1.55 μm wavelength from both the analytical model (theory) and numerical FEM simulations.

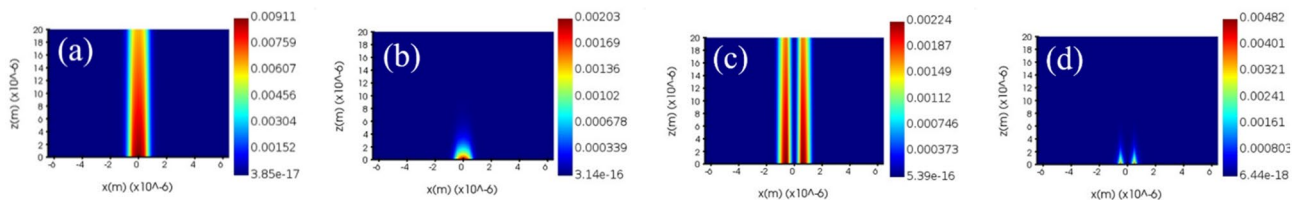


Figure 7. Optical power distribution along the length for the HE_{11} even mode (a, b) and TE_{01} (c, d) mode. Results are shown in the (a, c) amorphous and (b, d) crystalline GST phases. The optical power propagation in the cylindrical switch is analyzed to determine the required device length.

the optical power rapidly decays within 10 μm . Specifically, the optical power reduces by over 50% within just 1.2 μm and 1.05 μm for the HE_{11} and TE_{01} modes, respectively in crystalline GST. In contrast, the amorphous phase, optical power only drops around 5% over the same distance. Based on these results, switch lengths of 1.2 μm and 1.05 μm are chosen for the HE_{11} and TE_{01} modes respectively to enable efficient switching between crystalline and amorphous phases.

Electrical and thermal simulations

Phase change of GST can be induced by raising its temperature for a set time before cooling. This is typically achieved via optical or electrical stimulation⁴⁷. In this work, electrical stimulation is utilized for switching. Voltage applied to the gold layers causes current to flow through the GST, heating it up. The elevated temperature triggers the reversible transition between amorphous and crystalline phases. This switching allows the proposed cylindrical waveguide structure to selectively transmit or reflect certain wavelengths by altering the GST refractive index.

To simulate the electrical heating process, the heat transfer equation (Eq. 11) was coupled to the electric current equation (Eq. 12) using FEM⁴⁸.

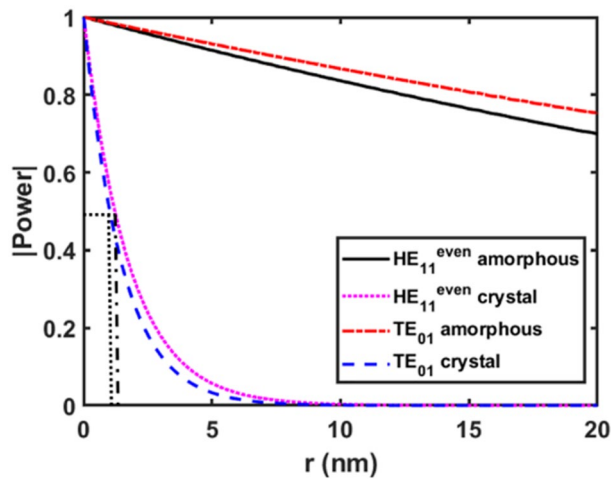


Figure 8. Simulated optical power distribution in the optimized switch design for the even HE_{11} and TE_{01} modes. Results are shown for the amorphous and crystalline GST phases. The power is plotted at the midpoint of the inner Si and outer Si layers, respectively.

$$\rho C_p \frac{dT}{dt} + \rho C_p u_{\text{trans}} \cdot \nabla T + \nabla \cdot (q + q_r) = -\alpha T \frac{dS}{dt} + Q \quad (11a)$$

$$Q = -\alpha T \frac{dS}{dt} \quad (11b)$$

where ρ is the density (kg/m^3), C_p is the heat capacity ($\text{J/kg}\cdot\text{K}$), k is the thermal conductivity ($\text{W/m}\cdot\text{K}$), T is the absolute temperature (K), u_{trans} is the translational velocity (m/s), q is the heat flux by conduction (W/m^2), q_r is the heat flux by radiation (W/m^2), α is the coefficient of thermal expansion ($1/\text{K}$), S is second Piola–Kirchhoff stress tensor (Pa), and Q is the additional heat sources (W/m^3). For steady-state conditions, the temperature is constant over time. Therefore, the transient heat transfer Eq. (11a) reduces to the steady-state form Eq. (11b).

To simulate joule heating in the phase change material, the electric current and heat transfer physics were coupled. The Poisson's equation [Eq. (12)] was used to calculate current distribution by the applied voltage. The heat transfer equation [Eq. (11)] then modeled thermal conduction and temperature distribution in the switch structure.

$$\nabla \cdot (\sigma \nabla V) = 0 \quad (12)$$

where σ is the electrical conductivity and V is the electric potential. By iteratively solving thermal-electrical model, the temperature profile arising from the applied voltage was determined. This enables predicting the amount of voltage requirements for phase change. As temperature variations induce phase change in the GST layer, the temperature-dependent properties of the Si, GST, and Au layers were entered into the concerned equations. This ensures accuracy when simulating across the wide temperature range required for amorphous to crystalline (or vice versa) switching. The electrical and thermal parameters of different layers are presented in supplementary.

Yu et al.⁴⁹ investigated the relationship between GST thickness and required switching time. Their findings indicate that for a 10 nm thick GST layer, the crystallization threshold temperature is 413 K, while the amorphization threshold temperature is 819 K. Thicker GST layers need longer dwell times above the crystallization temperature for phase change, decreasing the switching speed. Wang et al.⁵⁰ also studied the transient temperatures needed for amorphous-to-crystalline and crystalline-to-amorphous switching. Picosecond pulses can melt and quench crystalline GST into the amorphous phase since the atomic bonds do not have time to rearrange. However, nanosecond pulses are required for crystallization to allow resonant bonding. Meanwhile, experimental data were used for the temperature-dependent heat capacity, thermal conductivity, and electrical conductivity of gold layer, presented in supplementary^{51,52}.

Applying tailored electrical pulses allows temporally controlling the phase change in GST between amorphous and crystalline states. The pulse parameters for amorphous-to-crystalline switching are: source voltage $V_{\text{src}} = 5\text{V}$, offset voltage $V_{\text{off}} = 0\text{V}$, delay time $t_d = 0\text{ ns}$, rise time $t_r = 1\text{ ns}$, fall time $t_f = 1\text{ ns}$, pulse width $p_w = 140\text{ ns}$, and period $T_{\text{per}} = 300\text{ ns}$. For crystalline-to-amorphous transition, the parameters are: $V_{\text{src}} = 15\text{V}$, $t_r = 0.1\text{ ns}$, $t_f = 0.1\text{ ns}$, $p_w = 4\text{ ns}$, and $T_{\text{per}} = 100\text{ ns}$. Properly engineering the pulse amplitude, width, rise/fall times, and frequency induces the required transient temperature profile in the GST layer to enable reversible phase switching. The gold (Au) electrodes transport the electrical stimulus for Joule heating of the GST.

The electrical conductivity of crystalline GST is nearly 1000 times higher than amorphous GST. Therefore, a higher voltage pulse is required to switch from the crystalline to amorphous phase. Figure 9 shows the simulated current density distribution between the Au electrode layers during phase change. In the

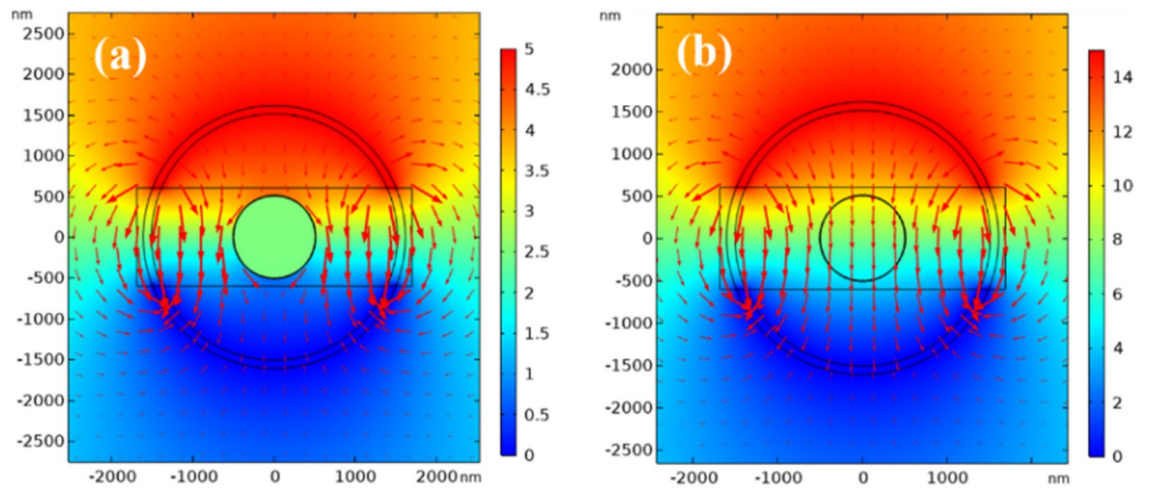


Figure 9. Electrical potential and current density (arrow) distributions in the cross-section of the optimized optical switch design during (a) amorphous-to-crystalline and (b) crystalline-to-amorphous phase transitions. The applied voltages are 5 V and 15 V, respectively.

amorphous-to-crystalline transition (Fig. 9a), a 5 V pulse produces high current density along the Au edges, with minimal current in the inner Si layer. However, for crystalline-to-amorphous switching at 15 V (Fig. 9b), uniform current density passes through both the GST and inner Si regions.

Figure 10 shows simulated temperature distribution in the cross-section of the optimized optical switch during amorphous-to-crystalline phase change. The layer dimensions match the optimized optical design with thicknesses of 500 nm, 10 nm, 1000 nm, 100 nm, and 1200 nm for the inner Si, GST, outer Si, Au, and gap, respectively. A 5V pulse with 140 ns width and 160 ns cooling time was applied to induce crystallization. As seen in Fig. 10a, the GST layer reaches ~ 400 K after 25 ns, below the 413 K crystallization threshold. At 40 ns the temperature of GST surpasses the 413 K threshold temperature (Fig. 10b). At 95 ns (Fig. 10c), the GST is heated well above the threshold to sustain crystallization, which requires maintaining an elevated temperature sufficiently above the threshold temperature. After 140 ns, the voltage is turned off and the structure cools for 160 ns (Fig. 10d) to stabilize the crystalline phase.

Figure 11 shows the applied voltage pulse and resulting temperature curve over time at different locations in the GST layer during crystallization. A 5V, 140 ns pulse heats the structure above the 413 K crystallization threshold. Due to the gap in the Au layer, the temperature is non-uniform angularly. Three representative points were analyzed in each 90° quadrant, with the quadrants being equivalent by symmetry. Points 1–3 (see Fig. 1a) correspond to the maximum, average, and minimum temperatures in the GST layer. The minimum heating time above threshold should be ~ 4 ns for a 10 nm GST⁴⁹. For times exceeding 100 ns, the temperatures at points 1–3 stabilize and remain above the threshold temperature. After turn-off the applied voltage, cooling returns the GST temperature to 293.15 K in 200 ns, which crystallize the GST layer.

Figure 12 shows the simulated temperature distribution during crystalline-to-amorphous phase change. The transient response differs from crystallization due to the distinct phase switching behavior. Upon applying a 15V pulse, the temperature rapidly peaks within 4 ns and then gradually cools down. By 70 ns, the temperature in both the GST and Si materials drops below 300 K, allowing the completion of the amorphization process. During the amorphization process, the gap region plays a crucial role by concentrating the electric field, potentially raising the temperature of the adjacent silicon and gold layers above their melting points, which could adversely affect the optical properties. However, the optimized 1200 nm gap thickness mitigates this issue, ensuring that the silicon and gold remain in the solid state, preserving the desired optical characteristics.

Figure 13 illustrates the temperature response at different locations within the GST layer. The amorphization process requires heating the GST material above its melting point of approximately 819 K. However, for rapid

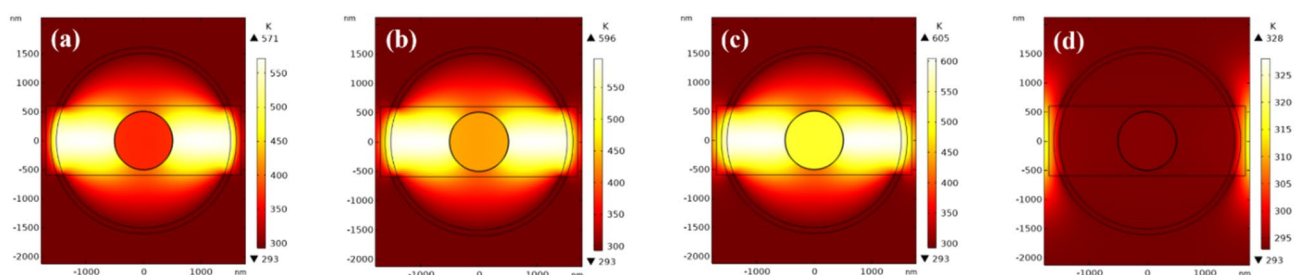


Figure 10. Temperature distribution in the cross-section of the optimized optical switch during amorphous-to-crystalline transition at times of (a) 25 ns, (b) 40 ns, (c) 95 ns, and (d) 270 ns.

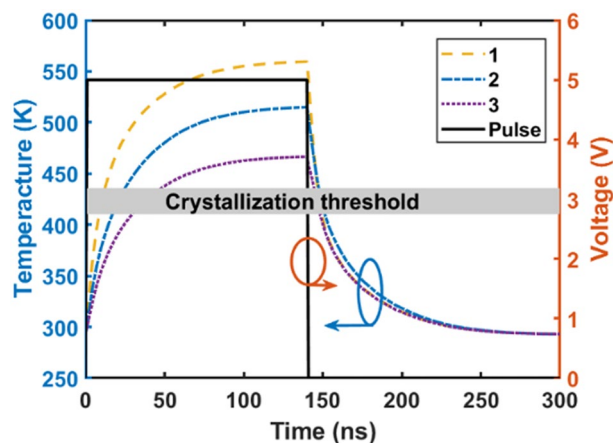


Figure 11. Applied voltage pulse and transient temperature profiles at points 1–3 (indicated in Fig. 1a) in the GST layer during crystallization. The thermal response exceeds the crystallization threshold for sufficient time to induce phase change.

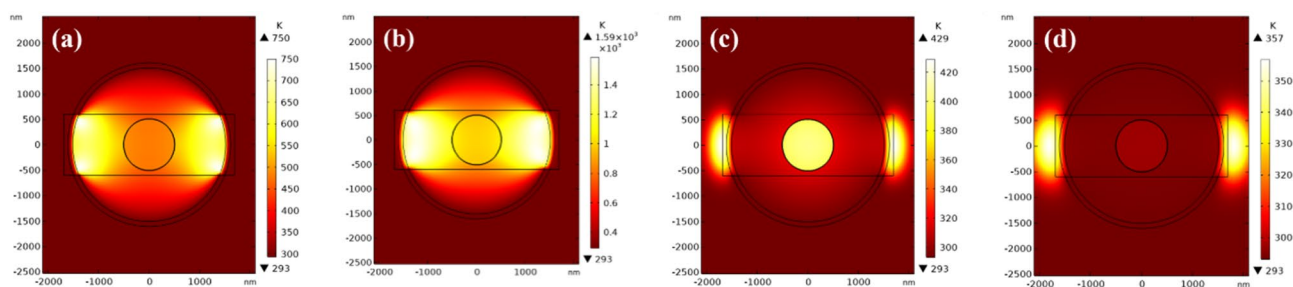


Figure 12. Temperature distribution in the cross-section of the optimized optical switch during crystalline-to-amorphous phase change at times of (a) 1 ns, (b) 4 ns, (c) 40 ns, and (d) 70 ns. The images reveal the transient thermal profile in the GST layer as it is heated above melting temperature and then cooled to stabilize the amorphous phase.

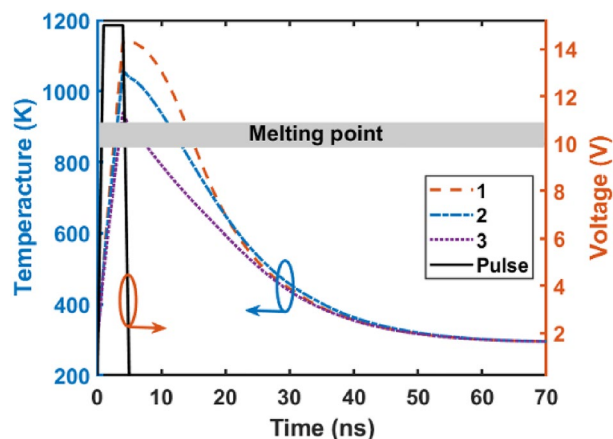


Figure 13. Applied voltage pulse and transient temperature profiles at points 1–3 (indicated in Fig. 1a) in the GST layer during crystalline-to-amorphous phase change. The thermal response exceeds the melting point of GST for sufficient time to induce amorphization.

Device	IL (dB)	ER (dB)	BR	EC	V or I
GST modulator ⁵³	18	5.7	2.86 Mb/s	–	–
GST modulator ⁴⁹	0.94	5.4	–	194 pJ	1 & 5 V
GST modulator ⁵⁴	0.95	–	1 Mb/s	–	5 & 15 V
GST modulator ⁵⁵	1.23	12.6	1.88 Mb/s	8.6 nJ	–
Proposed optical switch	0.79	13.47	3.5 Mb/s	30 nJ	5 & 15 V

Table 3. Comparison of simulated performance metrics for the proposed optical switch and other phase change modulators based on GST at 1550 nm wavelength.

amorphization on picosecond timescales, a higher applied voltage is necessary, as the atomic bonds within the material do not have sufficient time to rearrange at slower heating rates. Consequently, a 15 V, 4 ns pulse is applied, effectively heating the 10 nm GST layer above its melting point and enabling the amorphization process. Crucially, after 70 ns, all points within the GST layer cool below 300 K, facilitating the completion of the transition to the amorphous phase. This rapid cooling is essential to quench the disordered atomic structure and stabilize the material in the amorphous state, preventing undesired recrystallization.

Table 3 shows a comparison of simulation results for the proposed optical switch and some other modulators. The thermal simulation indicates that the optical switch has a bit rate of 3.5 MB/s at a wavelength of 1.55 μm . When the GST material switches between amorphous and crystalline phases, the maximum energy consumption is 30 nJ.

Conclusion

This work introduces a cylindrical waveguide optical switch using GST as an active phase change material on a silicon photonics platform. The phase change dynamics were analytically modeled and simulated using FEM. The TE_{01} and fundamental HE_{11} modes were studied to enable low-loss propagation in the amorphous phase and high extinction in crystalline GST. Increasing the GST thickness improved optical absorption but also slowed down switching kinetics, reducing modulation speeds. With a 10 nm GST layer, competitive performance was achieved with 0.79 dB insertion loss (IL), 13.47 dB extinction ratio (ER), 30 nJ average power consumption (EC), and 3.5 Mb/s bit rate (BR). Compared to prior GST-based modulators, some parameters are improved. This comprehensive multiphysics analysis of an architecturally novel, cylindrically symmetric GST-silicon optical switch represents a significant advance towards reconfigurable nanophotonics devices. The results provide a foundation for future work using phase change materials in integrated photonic circuits and optical communications.

Methods

The optical properties and performance of the proposed optical switch are analyzed using numerical techniques. 2D and 3D finite-element (FEM) and finite-difference time-domain (FDTD) methods are utilized to determine the modal and propagation characteristics, respectively. For FEM analysis of the modes, perfect electric conductor boundary conditions are applied at the exterior borders, with a tetrahedral mesh size of physics-controlled. The 3D FDTD simulation of light propagation employs perfectly matched layer (PML) outer boundaries and adaptive mesh refinement to minimize computation time and RAM requirements. Multiphysics electrical and thermal modeling utilizes 2D FEM, with thermally insulating boundaries and a triangular element mesh. Due to equation complexity, the analytical approach focuses only on the TE_{01} mode. By applying boundary conditions, the effective index is derived and the H_r field distribution is plotted. The analytical results are verified against FEM simulations, showing excellent agreement. Electrical current and thermal conduction physics are coupled for phase change simulations. The electrical and thermal properties of each layer determine the thermal profiles and amorphous-crystalline switching dynamics.

Data availability

The datasets used and/or analysed during the current study available from the corresponding author on reasonable request.

Received: 17 October 2023; Accepted: 6 May 2024

Published online: 10 May 2024

References

- Zhang, H., Yang, X., Chen, J., Rahman, B. M. A. & Zhou, L. Comparison of the phase change process in a GST-loaded silicon waveguide and MMI. *Opt. Express* **29**(3), 3503–3514 (2021).
- Bai, N. *et al.* A study on the crystallization behavior of Sn-doped amorphous $\text{Ge}_2\text{Sb}_2\text{Te}_5$ by ultraviolet laser radiation. *Appl. Surf. Sci.* **316**, 202–206 (2014).
- Xu, M. *et al.* Theoretical and experimental investigations of the optical properties of $\text{Ge}_2\text{Sb}_2\text{Te}_5$ for multi-state optical data storage. *J. Korean Phys. Soc.* **53**(4), 2265–2269 (2008).
- Hegedüs, J. & Elliott, S. R. Microscopic origin of the fast crystallization ability of Ge–Sb–Te phase-change memory materials. *Nat. Mater.* **7**(5), 399–405 (2008).
- Mittal, S. A survey of power management techniques for phase change memory. *Int. J. Computer Aided Eng. Technol.* **8**(4), 424–444 (2016).

6. Rudé Moreno, M. Micro-nano structured optical devices using Ge₂Sb₂Te₅. (Universitat Politècnica de Catalunya, 2016).
7. Pitchappa, P., Kumar, A., Prakash, S., Jani, H., Venkatesan, T., & Singh, R. Phase change-photonic framework for terahertz wave control. *arXiv preprint arXiv.1811.02729* (2018).
8. Zhang, Y. *et al.* Broadband transparent optical phase change materials for high-performance nonvolatile photonics. *Nat. Commun.* **10**(1), 4279 (2019).
9. Wuttig, M., Bhaskaran, H. & Taubner, T. Phase-change materials for non-volatile photonic applications. *Nat. Photon.* **11**(8), 465–476. <https://doi.org/10.1038/nphoton.2017.126> (2017).
10. Parra, J., Navarro-Arenas, J., Kovylyna, M. & Sanchis, P. Impact of GST thickness on GST-loaded silicon waveguides for optimal optical switching. *Sci. Rep.* **12**(1), 9774 (2022).
11. de Galarreta, C. R. *et al.* Tunable optical metasurfaces enabled by chalcogenide phase-change materials: from the visible to the THz. *J. Opt.* **22**(11), 114001 (2020).
12. Rui, G. *et al.* Symmetric Ge₂Sb₂Te₅ based metamaterial absorber induced dynamic wide-gamut structural color. *J. Opt.* **22**(8), 085003 (2020).
13. Chen, Y. *et al.* Engineering the phase front of light with phase-change material based planar lenses. *Sci. Rep.* **5**(1), 8660. <https://doi.org/10.1038/srep08660> (2015).
14. Michel, A. K. U. *et al.* Reversible optical switching of infrared antenna resonances with ultrathin phase-change layers using femtosecond laser pulses. *ACS Photon.* **1**(9), 833–839 (2014).
15. Wu, C. *et al.* Low-loss integrated photonic switch using subwavelength patterned phase change material. *ACS Photon.* **6**(1), 87–92 (2018).
16. Badri, S. H., Gilarlue, M. M., Farkoush, S. G. & Rhee, S. B. Reconfigurable bandpass optical filters based on subwavelength grating waveguides with a Ge₂Sb₂Te₅ cavity. *JOSA B* **38**(4), 1283–1289 (2021).
17. Kazanskiy, N. L., Butt, M. A. & Khonina, S. N. Optical computing: Status and perspectives. *Nanomaterials.* **12**(13), 2171. <https://doi.org/10.3390/nano12132171> (2021).
18. Ríos, C. *et al.* Integrated all-photonic non-volatile multi-level memory. *Nat. Photon.* **9**(11), 725–732. <https://doi.org/10.1038/nphoton.2015.182> (2015).
19. Wang, Y. *et al.* Electrical tuning of phase-change antennas and metasurfaces. *Nat. Nanotechnol.* **16**(6), 667–672. <https://doi.org/10.1038/s41565-021-00882-8> (2021).
20. Ahmadvand, A., Gerislioglu, B., Sinha, R., Karabiyik, M. & Pala, N. Optical switching using transition from dipolar to charge transfer plasmon modes in Ge₂Sb₂Te₅ bridged metalodielectric dimers. *Sci. Rep.* **7**(1), 42807. <https://doi.org/10.1038/srep42807> (2017).
21. Wu, D. *et al.* Resonant multilevel optical switching with phase change material GST. *Nanophotonics* **11**(15), 3437–3446. <https://doi.org/10.1515/nanoph-2022-0276> (2022).
22. Wei, M., Song, Z., Deng, Y., Liu, Y. & Chen, Q. Large-angle mid-infrared absorption switch enabled by polarization-independent GST metasurfaces. *Mater. Letters* **236**, 350–353 (2019).
23. Wang, N. *et al.* Design of ultra-compact optical memristive switches with GST as the active material. *Micromachines* **10**(7), 453. <https://doi.org/10.3390/mi10070453> (2019).
24. Mahmoodi, A., Miri, M., Sheikhi, M. H. & Pouyan, S. M. Design of high extinction ratio, low loss, and compact optical modulators and switches based on GST phase change material. *JOSA B.* **38**(11), 3261–3268 (2021).
25. Snyder, W. A. & Sammut, R. A. Fundamental (HE₁₁) modes of graded optical fibers. *J. Opt. Soc. Am.* <https://doi.org/10.1364/JOSA.69.001663> (1979).
26. Snyder, W. A. & Young, W. R. Modes of optical waveguides. *J. Opt. Soc. Am.* <https://doi.org/10.1364/JOSA.68.000297> (1978).
27. Dragone, C. Attenuation and radiation characteristics of the HE₁₁ mode. *IEEE Trans. Microw. Theory Tech.* **28**(7), 704–710. <https://doi.org/10.1109/TMTT.1980.1130152> (1980).
28. Xu, G., Zhang, W., Huang, Y. & Peng, J. Loss Characteristics of Single-HE₁₁-Mode Bragg Fiber. *J. Lightwave Technol.* **25**, 359–366 (2007).
29. Chou, C. C. & Sun, N. H. Analysis of leaky-mode losses for optical fibers. *J. Opt. Soc. Am. B.* <https://doi.org/10.1364/JOSAB.25.000545> (2008).
30. Salzberg, C. D. & Villa, J. J. Infrared refractive indexes of silicon germanium and modified selenium glass. *JOSA* **47**(3), 244–246 (1957).
31. Tatian, B. Fitting refractive-index data with the Sellmeier dispersion formula. *Appl. Opt.* **23**(24), 4477–4485 (1984).
32. Frey, B. J., Leviton, D. B. & Madison, T. J. Temperature-dependent refractive index of silicon and germanium. *Optomech. Technol. Astron.* <https://doi.org/10.1117/12672850> (2006).
33. Moghaddam, S. & O’Leary, S. K. A Sellmeier extended empirical model for the spectral dependence of the refractive index applied to the case of thin-film silicon and some of its more common alloys. *J. Mater. Sci. Mater. Electron.* **31**, 212–225. <https://doi.org/10.1007/s10854-019-02457-9> (2020).
34. Aliqab, K. *et al.* Numerical analysis of Phase change material and graphene-based tunable refractive index sensor for infrared frequency spectrum. *Sci. Rep.* **13**, 7653. <https://doi.org/10.1038/s41598-023-34859-5> (2023).
35. Liang, H. *et al.* Simulations of silicon-on-insulator channel-waveguide electrooptical 2×2 switches and 1×1 modulators using a Ge₂Sb₂Te₅ self-holding layer. *J. Lightwave Technol.* **33**(9), 1805–1813 (2015).
36. Shportko, K. *et al.* Resonant bonding in crystalline phase-change materials. *Nat. Mater.* **7**(8), 653–658. <https://doi.org/10.1038/nmat2226> (2008).
37. Sarangan, A. *et al.* Broadband reflective optical limiter Using GST phase change material. *IEEE Photon. J.* **10**(2), 1–9. <https://doi.org/10.1109/JPHOT.2018.2796448> (2018).
38. Rakić, A. D., Djurišić, A. B., Elazar, J. M. & Majewski, M. L. Optical properties of metallic films for vertical-cavity optoelectronic devices. *Appl. Opt.* **37**(22), 5271–5283 (1998).
39. Johnson, P. B. & Christy, R. W. Optical constants of the noble metals. *Phys. Rev. B.* <https://doi.org/10.1103/PhysRevB.6.4370> (1972).
40. Olmon, R. L. *et al.* Optical dielectric function of gold. *Phys. Rev. B* <https://doi.org/10.1103/PhysRevB.86.235147> (2022).
41. Gao, L., Lemarchand, F. & Lequime, M. Exploitation of multiple incidences spectrometric measurements for thin film reverse engineering. *Opt. Express* **20**(14), 15734–15751 (2012).
42. Malitson, I. H. Interspecimen comparison of the refractive index of fused silica. *Josa* **55**(10), 1205–1209. <https://doi.org/10.1364/JOSA.55.001205> (1965).
43. Qayoom, T. & Najeeb-ud-din, H. Effective index approximation based analytical modeling and two dimensional numerical investigation of surface and bulk sensitivity in optimized hybrid nanostructured plasmonic gratings with miniaturized footprints. *Opt. Quantum Electron.* **55**(4), 302. <https://doi.org/10.1007/s11082-023-04592-4> (2023).
44. Palpant, B., Guillet, Y., Rashidi-Huyeh, M. & Prot, D. Gold nanoparticle assemblies: Thermal behaviour under optical excitation. *Gold Bull.* **41**, 105–115 (2008).
45. Prakash, C. Thermal conductivity variation of silicon with temperature. *Microelectron. Reliab.* **18**(4), 333 (1978).
46. Guo, P., Sarangan, A. M. & Agha, I. A review of germanium-antimony-telluride phase change materials for non-volatile memories and optical modulators. *Appl. Sci.* **9**(3), 530 (2019).
47. Xu, Q., Schmidt, B., Pradhan, S. & Lipson, M. Micrometer-scale silicon electro-optic modulator. *Nature* **435**(7040), 325–327 (2005).
48. https://doc.comsol.com/5.5/doc/com.comsol.help.heat/heat Ug_theory.07.07.html

49. Yu, Z., Zheng, J., Xu, P., Zhang, W. & Wu, Y. Ultracompact electro-optical modulator-based Ge₂Sb₂Te₅ on silicon. *IEEE Photon. Technol. Letters* **30**(3), 250–253 (2017).
50. Wang, W. J. *et al.* Fast phase transitions induced by picosecond electrical pulses on phase change memory cells. *Appl. Physics Letters* <https://doi.org/10.1063/12963196> (2008).
51. Takahashi, Y. & Akiyama, H. Heat capacity of gold from 80 to 1000 K. *Thermochimica Acta* **109**(1), 105–109 (1986).
52. Haynes, W. M. (ed.) *CRC handbook of chemistry and physics* (CRC Press, 2014).
53. Ikuma, Y. *et al.* Reversible optical gate switching in Si wire waveguide integrated with Ge₂Sb₂Te₅ thin film. *Electronics Letters* **46**(21), 1460–1462 (2010).
54. Liang, H. *et al.* Simulations of silicon-on-insulator channel-waveguide electrooptical 2×2 switches and 1×1 modulators using a Ge₂Sb₂Te₅ self-holding layer. *J. Lightwave Technol.* **33**(9), 1805–1813 (2015).
55. Tanaka, D. *et al.* Ultra-small, self-holding, optical gate switch using Ge₂Sb₂Te₅ with a multi-mode Si waveguide. *Optics Express* **20**(9), 10283–10294 (2012).

Author contributions

All authors contributed extensively to the study presented in this paper. Conceptualization, M.N., S.A. and A.M.M.; methodology, M.N.; software, A.M.M.; validation, M.N., S.A. and A.M.M.; formal analysis, A.M.M. and M.N.; writing—original draft preparation, S.A.; writing—review and editing, M.N., S.A. and A.M.M.; supervision, M.N.; project administration, M.N.

Competing interests

The authors declare no competing interests.

Additional information

Supplementary Information The online version contains supplementary material available at <https://doi.org/10.1038/s41598-024-61473-w>.

Correspondence and requests for materials should be addressed to M.N.

Reprints and permissions information is available at www.nature.com/reprints.

Publisher's note Springer Nature remains neutral with regard to jurisdictional claims in published maps and institutional affiliations.



Open Access This article is licensed under a Creative Commons Attribution 4.0 International License, which permits use, sharing, adaptation, distribution and reproduction in any medium or format, as long as you give appropriate credit to the original author(s) and the source, provide a link to the Creative Commons licence, and indicate if changes were made. The images or other third party material in this article are included in the article's Creative Commons licence, unless indicated otherwise in a credit line to the material. If material is not included in the article's Creative Commons licence and your intended use is not permitted by statutory regulation or exceeds the permitted use, you will need to obtain permission directly from the copyright holder. To view a copy of this licence, visit <http://creativecommons.org/licenses/by/4.0/>.

© The Author(s) 2024